

ORIGINAL ARTICLE

A Fully Three-Dimensional Printed Inchworm-Inspired Soft Robot with Magnetic Actuation

Erina B. Joyee and Yayue Pan

Abstract

In the field of robotics, researchers are aiming to develop soft or partially soft bodied robots that utilize the motion and control system of various living organisms in nature. These robots have the potential to be robust and versatile, even safer for human interaction compared to traditional rigid robots. Soft robots based on biomimetic principles are being designed for real life applications by paying attention to different shape, geometry, and actuation systems in these organisms that respond to surrounding environments and stimuli. Especially, caterpillars or inchworms have garnered attention due to their soft compliant structure and crawling locomotion system making them ideal for maneuvering in congested spaces as a transport function. Currently, there are two major challenges with design and fabrication of such soft robots: using an efficient actuation system and developing a simple manufacturing process. Different actuation systems have been explored, which include shape memory alloy based coils and hydraulic and pneumatic actuators. However, the intrinsic limitations due to overall size and control system of these actuators prevent their integration in flexibility, lightweight, and compact manner, limiting practical and untethered applications. In comparison, magnetic actuation demonstrates simple wireless noncontact control. In terms of manufacturing process, additive manufacturing has emerged as an effective tool for obtaining structural complexity with high resolution, accuracy, and desired geometry. This study proposes a fully three-dimensional (3D) printed, monolithic, and tetherless inchworm-inspired soft robot that uses magnetic actuation for linear locomotion and crawling. Its structure is multimaterial heterogeneous particle–polymer composite with locally programmed material compositions. This soft robot is directly printed in one piece from a 3D computer model, without any manual assembly or complex processing steps, and it can be controlled by an external wireless force. This article presents its design and manufacturing with the novel magnetic field assisted projection stereolithography technique. Analytical models and numerical simulations of the crawling locomotion of the soft robot are also presented and compared with the experimental results of the 3D printed prototype. The overall locomotion mechanism of the magnetically actuated soft robot is evaluated with friction tests and stride efficiency analysis.

Keywords: 3D printing, bio-inspired soft robotics, magnetic actuation, crawling locomotion, particle–polymer composite, stereolithography

Introduction

ADVANCES IN MATERIAL SCIENCE, accumulative understandings of biology, and recent developments in manufacturing technology and simulation platforms have greatly benefited the field of soft robotics.^{1–3} Especially, emerging digital fabrication technologies like additive manufacturing are allowing design and fabrication of soft robots with superior structural complexity at a large scale and with fewer materials.

Many studies took inspiration from soft bodied insect larvae like caterpillars and inchworms with crawling and inching locomotion systems.^{2,4–7} These insects have fully soft compliant bodies without any rigid components (e.g., skeletons), and they exhibit unprecedented abilities in adapting shape, morphology, and locomotion behaviors by conjugating neural control process and biomechanics,^{5,7–10} making them ideal for applications that increased adaptability, safety, and complex motions which would be quite difficult for traditional robots.^{1,11}

Researchers have focused on incorporating smart actuators to compliant materials to provide the driving force and control mechanism of the soft robot. Actuators that have been incorporated into soft robots include shape memory alloys (SMAs),^{6,12–14} pneumatics,^{15–18} hydraulic,^{10,19,20} motor-tendons,²¹ and thermal-electroactive polymers.^{22–24} For example, recent studies used SMA actuators to develop soft robots mimicking movements and locomotion of jellyfish,¹⁴ marine turtle,²⁵ octopus,²⁶ and soft bodied fish.²⁷ Umedachi *et al.* demonstrated an electrically powered SMA actuated deformable robot, which was capable of crawling and steering with a reasonable speed.⁶ This robot was produced by fabricating parts using a three-dimensional (3D) printing technique and then manually assembling the parts with SMA coils. Wang *et al.* also demonstrated a similar SMA based soft robot that was fabricated by molding, manual assembly, and a few postprocessing steps.⁵ In both cases, the manufacturing processes were very time consuming, and the manual assembly limited the achievable size, geometry, resolution, and accuracy. Furthermore, SMA actuated structures mostly become complicated and trouble prone with arduous direction control and wired interface with the robot body, significantly restricting the use of soft robots in delicate and sophisticated environment (i.e., inside living body). As an alternative to SMA based actuators, some studies used pneumatic and hydraulic actuation systems.^{15,16,19} However, pressure regulating components and external compressors for pneumatic and hydraulic actuators also limit miniaturized and untethered practical applications.²⁸ Ueno *et al.* demonstrated an inchworm based bidirectional soft robot and used electro-conjugate fluid (ECF) to produce its body deformation and contraction at the robot's feet.²⁹ But the robot had to be connected externally to an ECF tank and required high voltage.

Another alternative magnetic actuation provides a non-contact approach, which circumvents the issues associated with SMA based actuation, hydraulic, or pneumatic actuation systems.³⁰ With proper magnetic environment, magnetic actuation can be operated in different mediums, including air, vacuum, and liquids.^{30,31} The flexibility of magnetic actuation combined with advantages of polymer composites makes it really attractive for soft robot applications. Saga and Nakamura, *et al.*, for example, proposed a peristaltic crawling robot controlled by a moving magnetic field, which showed good locomotion performance in congested spaces.³² The robot was constructed by manual assembly of cells filled with magneto fluids. Such magneto fluid cell assembly design allowed noncontact magnetic actuation; however, the manufacturing and actuation process were complex and time consuming.

From the review of the literature, it can be concluded that there exists a knowledge gap on how to design a robust soft robot with an efficient actuation system that can be easily fabricated using a simple manufacturing process. In this study, we propose an inchworm-inspired soft monolithic robot, which is constructed by 3D printed smart particle-polymer composites with locally controlled material compositions and hence can be actuated by magnetic fields. Different from the existing soft robots that need to assemble the robot body with certain actuators, our proposed manufacturing method programmed the actuation intelligence in the material design of the soft robot. Our soft robot is

a smart particle-polymer composite object that is 3D printed in one piece, directly from the digital model, and requires no manual assembly or pre-post processing steps and has locally programmed magnetic particle distributions which attribute to its magnetic actuation intelligence. With the locally controlled magnetic particle distribution, the particle-polymer composite robot uses an anchor push-anchor pull locomotion strategy mimicking the inchworm and is capable of two-way linear actuation.

This study demonstrates multimaterial monolithic soft robots, 3D printed by a novel magnetic field-assisted projection stereolithography (M-PSL) process. The magnetic actuation system of the soft robot was analytically modeled and simulated in COMSOL Multiphysics, and the simulation results guided the settings for experimental locomotion parameters. Experiments have been conducted in various complicated scenarios, such as regular construction paper surface, rough sandpaper surface, and inclined surface, through a congested tube and in a complex maze structure. Stride efficiency analysis and friction tests were also conducted to evaluate and validate the performance of the magnetically actuated 3D printed smart composite soft robot, compared to the locomotion of an inchworm in nature.

The rest of the article is organized as follows: the “Bio-Inspiration for the Soft Robot” section describes the bio-inspiration from inchworm and the analysis of its steering mechanism; “Design and Manufacturing of a Smart Polymer Composite Soft Robot” section describes the overall design, fabrication, and locomotion principle of the 3D printed smart composite robot with details of the COMSOL simulation; “Experimental Result and Discussion” section describes simulation results and discusses the experimental performance of the printed robot; and finally “Conclusions” section summarizes this study and its findings.

Bio-Inspiration for the Soft Robot

In contrast with living animals with rigid skeletons, soft-bodied animals like caterpillars or earthworms have the lesser limitation on movement and adapting their shape and morphology. They can deform their soft and compliant bodies with a large degree of freedom and demonstrate the use of strong muscular pressure. An example of such soft-bodied animals is an inchworm. They are caterpillars of the geometer moth with long sarcomeres and few pairs of prolegs. It has single innervated muscles with no constricted body segments.⁶ It crawls through segments of wave-like contractions from posterior to anterior section. Such body structure of the inchworm inspired our design of the soft robot, which has a soft monolithic body without any segments and follows a push-pull locomotion strategy. Same as the inchworm, the surface contact of our robot is maintained only with its legs, not the whole body. This also corresponds to the natural terrestrial movement of inchworms which has a comparatively slow speed compared to mollusks and worms. The proposed soft robot in this article has mainly taken inspiration from the locomotion and soft bodied geometry of an inchworm. The following sections describe the crawling mechanism and inherent friction control of the soft robot and how they are inspired from inchworms.

Crawling mechanism

Inchworms utilize an effective crawling locomotion strategy with their posterior and anterior true legs.⁹ The legs at the two ends create a two state, high-low friction for locomotion and function as actuators. As the longitudinal muscles contract, the body of the inchworm bends and with alternating immobilization of the posterior and anterior legs, it creates a looping gait for locomotion. For linear crawling, the actuation of the legs and contraction of the muscle fibers are usually symmetric. In case of steering or turning locomotion, the muscles of the inchworms contract asymmetrically, which cause the worm body to move in an angular direction. However, for both linear and turning movements, the anchor push-pull strategy is the same. While the body bends uniaxially in forward-backward movements, it moves biaxially in turning movements.

We examined the natural movement of an inchworm and observed multiple crawling positions which are taken by the worm to crawl forward by one step. These positions are efficient as they need minimal space and also help the insect to move forward.^{5,9} The inchworm repeats these optimized crawling cycles for certain number of times until it reaches its destination.

A simple way to prove the repetition of this movement cycle is to measure the curvature of its body in various positions and compare them for multiple cycles. The curvature of the inchworm's body can be quantified by comparing the geodesic distance with Euclidean distance between its posterior and anterior legs. Figure 1a illustrates schematic of an inchworm and shows how curvature is measured in the yz plane. For different arc-like positions of the inchworm, we identified the posterior and anterior legs as two endpoints and segmented the virtual skeleton of the

body to measure the curvature. From the two ends, the calculated curvature is

$$Curvature = \frac{1}{n} \sum_{i=1}^n \frac{Geodesic\ distance\ between\ two\ endpoints}{Euclidean\ distance\ between\ two\ endpoints} \quad (1)$$

If the body is considered as a curve $C = (y(t), z(t))$ with time (t) in an interval $[t_0, t_1]$,

Geodesic distance can be calculated as an integral as follows,

$$Geodesic\ distance = \int_{t_0}^{t_1} \sqrt{\left(\frac{dy(t)}{dt}\right)^2 + \left(\frac{dz(t)}{dt}\right)^2} dt \quad (2)$$

and Euclidean distance can be calculated as

$$Euclidean\ distance = \sqrt{(y_{t1} - y_{t0})^2 + (z_{t1} - z_{t0})^2} \quad (3)$$

We can observe the curvature difference in different frames, as shown in Figure 1b-e, which compares the initial position (position 1, Fig. 1b, d) and position at the highest curvature (position 3, Fig. 1c, e). As the initial position is relatively flat, the geodesic distance is smaller and almost similar to Euclidean distance. In contrast, during its crawling cycle, when the worm has the highest curvature the geodesic distance is quite high.

To compare the curvature of different crawling positions quantitatively, five crawling cycles of a real inchworm were observed and five consequent arc-like positions were selected

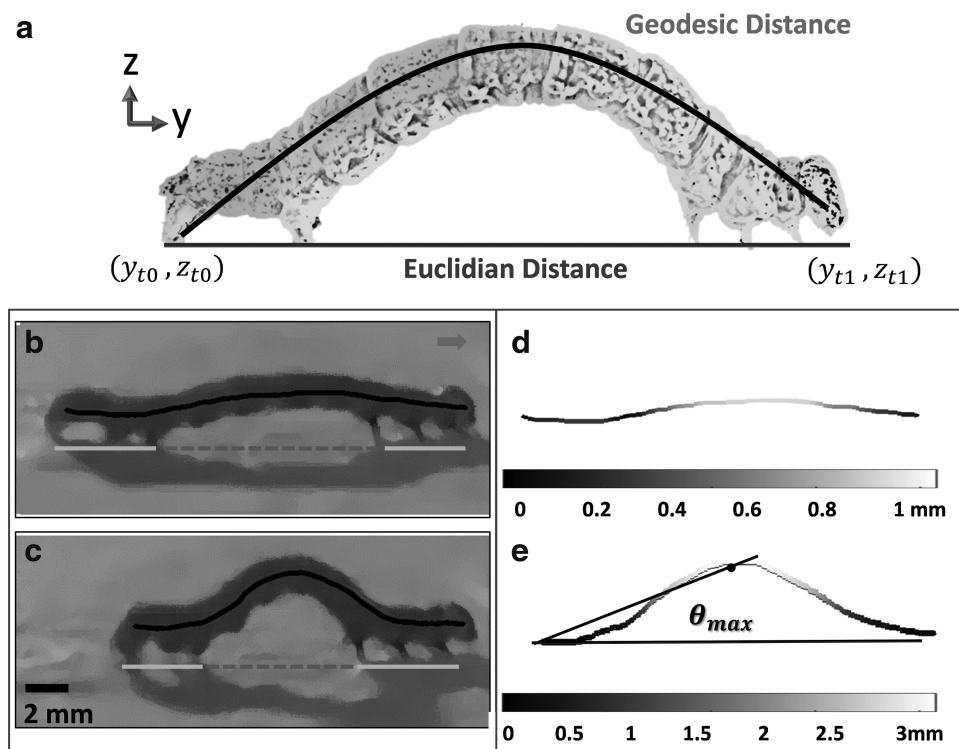


FIG. 1. (a) Illustration of Geodesic and Euclidean distances. (b-e) Comparison between curvatures of two different frames. (b, d) Illustrates initial crawling position (Pos 1). (c, e) Illustrates crawling position at the highest curvature (Pos 3).

for each cycle. The measured curvature values of different positions (positions 1–5) are shown in Table 1. We can observe from Table 1 that the mean curvature of the five positions in five cycles has small standard deviations, implying that, for all the crawling cycles, the curvature in the five positions is similar. This proves that the worm uses positions like these to complete a crawling cycle and repeats the cycle to complete its journey. The mean curvature of positions 1, 2, and 3 is significantly different from each other. The p -value for statistical ANOVA among positions 1, 2, and 3 was smaller than 0.001 for all cases. For the anchor-push locomotion during forward movement, the inchworm uses the combination of positions 1, 2, and 3. At position 3, the curvature is the highest, and the value starts decreasing to positions 4 and 5 consecutively. The latter part is called anchor-pull locomotion, which concludes the forward motion crawling cycle.

Our proposed soft robot adapts a similar push–pull locomotion strategy as the nature of inchworm for linear movements, mimicking the five bending positions detailed in the Table 1. However, the bending capability of our robot is limited to y axis (forward and back) only. So in case of steering left or right in x axis, the body mostly relies on the magnetic field actuation direction while maintaining push–pull locomotion strategy. This requires a comparatively larger space to turn for the robot. However, our soft robot is a pilot prototype that demonstrates the monolithic design with smart polymer composites and magnetic actuation based push–pull locomotion. In the future prototype, we plan to modify the robot design to enable turning locomotion and a more efficient steering control.

Inherent friction control

The inchworm has a very effective and unique gripping mechanism with legs and soft membranes beneath them. There are previous literatures which have extensively studied the gripping and biomechanics of prolegs of different types of caterpillars.^{33–39} The prolegs are essential for inching and crawling locomotion as described by Van Griethuijsen and Trimmer.³⁵ However, a coordination of proleg grip and re-

lease with a wave-like muscle activity is required for forward or turning movement.³⁷ Caterpillars such as *Manduca sexta* grip the surface beneath them with prolegs as anchors and lift them during the movement of the whole body segment during muscle retraction.³³ Mukherjee *et al.*³⁴ hypothesize that proleg grip release is a function of active neural control and local mechanical control. So basically, a caterpillar or, in our case, an inchworm grips the underlying surface and creates alternating high and low friction states for locomotion using their prolegs and body muscles (sarcomeres). Umedachi *et al.*,⁶ considered these states of friction as a function of contact angle between prolegs and substrates. This study adapted a similar strategy and designed the change of friction states as a function of the tilt angles (θ) between the direction of posterior leg and underlying substrate. As shown in Figure 1e, it can be observed that the angle is the highest when the curvature is the maximum. This angle is called the threshold angle (θ_{\max}).⁶ The body of the inchworm has the minimum friction with the substrate when the curvature and tilt angle are the maximum. At its resting state, the friction is the maximum. The locomotion of the worm is conducted through switching between the two friction states.^{5,6}

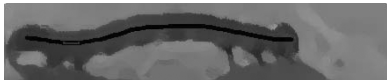
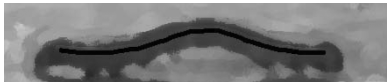
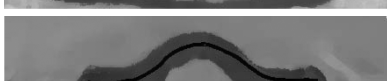
This friction alternating locomotion mechanism has been characterized by calculating the values of curvatures and corresponding tilt angles. At the highest curvature position, the threshold angle (θ_{\max}) was calculated as shown in Figure 1e. The measured threshold angle in Figure 1e was 21.5°. In this study, the soft robot was designed to mimic the movement of the inchworm and follow the measured bending deformation and threshold angles of the inchworm. Further details about the design, manufacturing, and actuation control of the soft robot are given in the following sections.

Design and Manufacturing of a Smart Polymer Composite Soft Robot

Digital model of the particle–polymer composite soft robot

The robot body has a smart particle–polymer composite structure with magnetic particles embedded in the anterior

TABLE 1. COMPARISON OF CURVATURE AMONG DIFFERENT CRAWLING POSITIONS

Positions	Mean curvature (five cycles)	Standard deviations	Crawling positions
1	1.01	0.01	
2	1.16	0.02	
3	1.29	0.03	
4	1.14	0.03	
5	1.03	0.01	

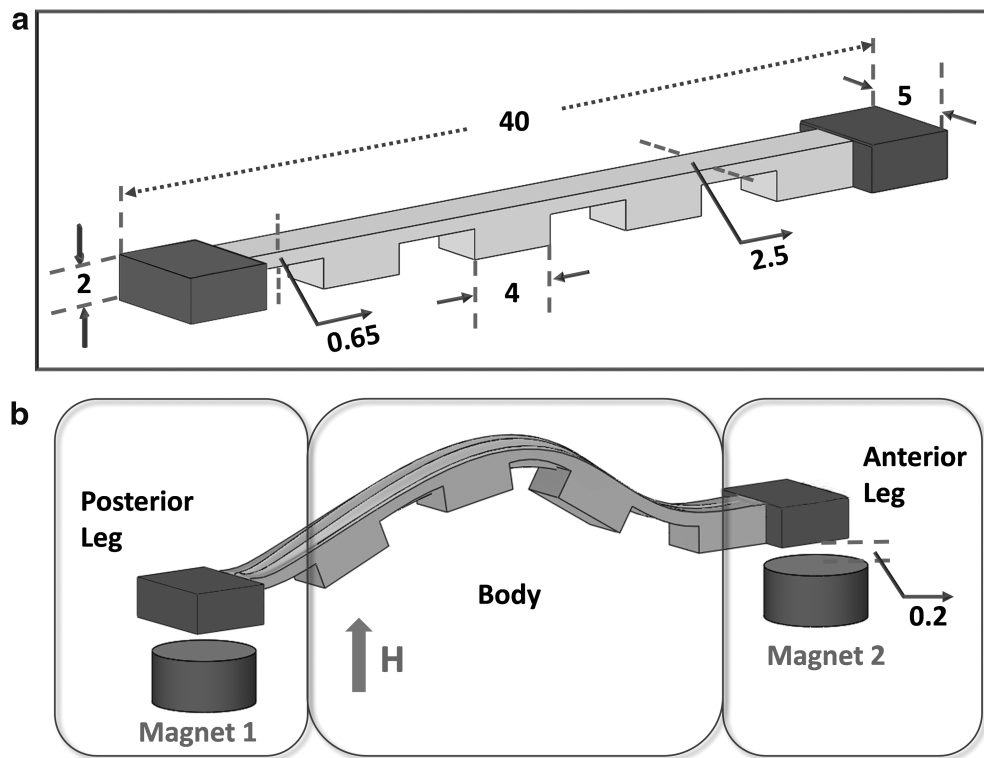


FIG. 2. (a) CAD model of the soft robot with all the dimensions (unit: mm). Different material compositions are shown by different colors in the schematic, *dark gray*: magnetic particle–polymer composite, *light gray*: flexible polymer, (b) CAD model showing posterior and anterior magnets placed at two legs. CAD, computer-aided design.

and posterior leg, working as actuators. A schematic of the digital model is shown in Figure 2a. The flexible polymer allows it to be highly deformable with a high friction coefficient.^{5,6} The posterior and anterior segments take on a cubic shape to allow a synchronized movement with a moving magnetic field.

The computer-aided design (CAD) model of the soft robot was created in SolidWorks (version 2016; Concord, MA, UA). The length of the robot is 40 mm with two actuator legs at the posterior and anterior ends. These legs also help the robot to grip the underlying surfaces. The upper surface of the robot body is flat, and the lower surface has transverse rectangular ridges that act as supporting legs along the length of the body. The thickness of the main body and the legs is 0.65 and 2 mm, respectively. For our robot, the primary displacement was in xy plane with bending of the body in z direction and a dynamic angular orientation, θ .

Soft robot manufacturing using M-PSL

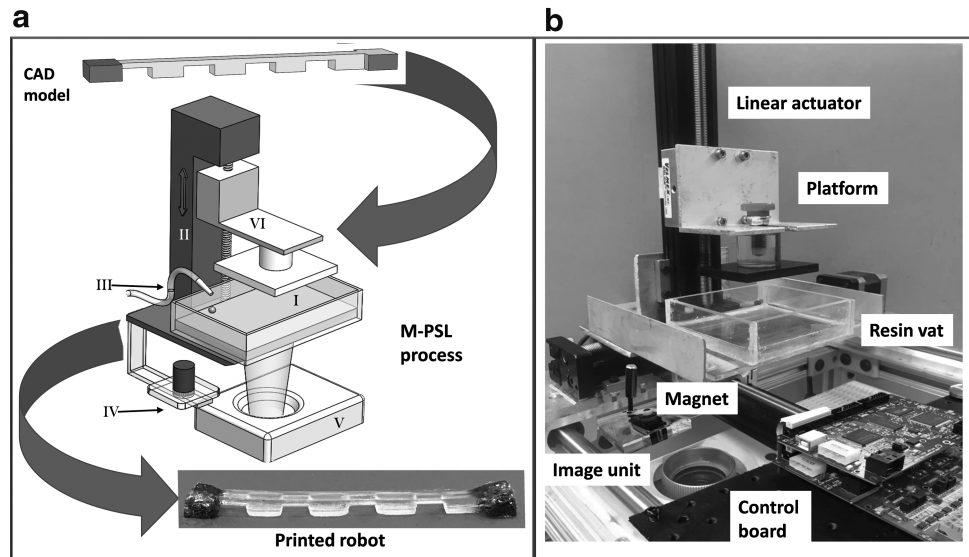
M-PSL process is a type of additive manufacturing process that can fabricate particle–polymer composites directly from digital model in a layer by layer manner, with locally controlled magnetic particle distributions.⁴⁰ A prototype machine was developed for implementing the fabrication process of particle–polymer composites. In the system, an external magnetic field is used to control particle dispersion and local distribution ratios. Figure 3a illustrates the overall M-PSL printing process and the experimental setup. A photograph of the real-life M-PSL prototype is shown in

Figure 3b. To print the designed soft robot, the CAD model was sliced into a set of two-dimensional layers along the z direction with a thickness of 0.2 mm. These slices were converted to digital mask images that were projected as patterned light to selectively expose and harden the resin. Two sets of mask images, the deposition and curing images, were used to fully cure the liquid resin and the particle-resin mixture.

In our experiment, Spot E from Spot A Materials (Barcelona, Spain) was used as the flexible resin. According to the literature, an ideal material for fabricating soft and compliant body structures should have elastic modulus of around 10^4 – 10^9 Pa and hardness in the range of shore A scale 30.^{41–43} This makes Spot E a perfect material for applications requiring soft but resilient materials as it demonstrates an exceptional toughness (10 MPa, equivalent to D19 hardness) and up to 65% elongation behavior (ISO 527–1A standard) after being cured. Synthetic black iron oxide nanoparticles (Alpha Chemical, MO) with 300 nm average diameter were mixed with Spot E base resin to prepare the magnetic field responsive smart polymer composites. The specific surface area of the spherical particles was $7.0 \text{ m}^2/\text{g}$.

A micronozzle and an external magnetic field were programmed into the experimental setup for controlling the deposition of magnetic particles. To fabricate a layer that has magnetic particles embedded, the dispensing system of the printer started depositing particles in the resin vat. After particle deposition, the corresponding deposition mask image was projected by the imaging unit to the particle filling region for a certain amount of time. The curing image was then projected to illuminate the whole cross-sectional plane of that

FIG. 3. (a) A schematic diagram of the robot printing system using M-PSL process, (b) M-PSL prototype. (I) Resin vat (II) linear actuator (III) particle dispensing system (IV) magnet with holder slide (V) image unit (VI) platform. M-PSL, magnetic field-assisted projection stereolithography.



layer. To fabricate a layer that has no particles embedded, after recoating a new layer of liquid resin between the part or the platform and the bottom surface of the resin vat, the curing image was projected directly to the liquid resin for a certain time to cure that layer. After a layer was cured, the platform separated the newly cured layer from the bottom surface of the resin vat, and a new layer of liquid resin would fill into the gap created between the cured layer and the bottom surface for the next layer fabrication. The platform was controlled by a microcontroller. By repeating this process, 3D soft robot with embedded magnetic particles was fabricated in the setup. The appropriate layer thickness and curing time were selected based on our previous study of the relationship between the curing depth and the magnetic particle loading fraction.⁴⁴ The volume loading fraction of the magnetic particles in the two legs was 37.34%.

Locomotion principle of 3D printed robot

This study proposes to model this crawling phenomenon with sequential activation of magnetic forces in the anterior and posterior legs of the robot with the help of two permanent magnets in corresponding legs (illustrated in Fig. 2b). The robot body is made of soft polymer that acts as muscle tissue, and the posterior and anterior ends are loaded with magnetic material that helps the two ends act as prolegs actuated by magnetic field. The legs create high-low states of friction with the substrate to create push-pull crawling locomotion. Locomotion principles in robotics and its relation with friction have been studied in detail in previous works of literatures.^{45,46}

At the resting phase, the robot is static and has a high friction with the substrate. At the beginning of the crawling cycle (pos 1), the posterior magnet (magnet 1) is mechanically moved in the y direction. The posterior leg is influenced by the magnet and pushed forward. The body of the robot bends at a tilt angle θ . The anterior leg at this point has a high friction with the substrate and is influenced by the anterior magnet (magnet 2), hence staying static. Without the magnet 2 acting as the anchor for the anterior leg, the body would return to its original configuration through elastic and grav-

itational potential energies. As the curvature of the robot increases, the tilt angle of the posterior leg with the substrate increases. As it reaches the maximum tilt angle (threshold angle, θ_{\max}), the friction decreases to its lowest point. At this stage, the magnet 2 moves forward in y direction and pulls the anterior leg with it. As the body continues to return to its original position, the tilt angle becomes smaller than the threshold angle. When the tilt angle reaches its minimum, the anterior leg movement stops and the posterior leg movements initiate again for further forward locomotion. The proposed soft robot prototype is not capable of bending in two dimensions (i.e., both z and x axes), which would allow turning locomotion using asymmetrical contraction of its soft polymer body. The current design only allows bending in z direction and forward-back movement in y direction. However, it is still able to steer in the xy plane but that process is solely dependent on the mechanical movement of magnets 1 and 2 and the corresponding magnetic actuation force created by them. As the magnets act as anchors to the posterior and anterior legs, the magnets can be moved in xy plane to steer the turning motion of the soft worm robot. However, this requires a large space to turn the robot and thus limits turning (sharp turn or U-turn) locomotion in a very congested area.

COMSOL Multiphysics simulation

To validate the effectiveness of the proposed magnetic field actuated locomotion process, crawling locomotion was simulated in COMSOL Multiphysics modeling software package (COMSOL, Inc.) using the AC/DC module as a continuum model.⁴⁷⁻⁴⁹ To create a realistic environment, a 3D air medium was selected for the simulation with a temperature of 293.15 K and a pressure of 1 atm.

The CAD model of the soft robot was imported to COMSOL, and the geometry was set accordingly. The posterior and anterior legs had iron oxide particles embedded in polymer, and the rest of the body was defined as pure polymer resin. These material properties were manually set in COMSOL material module. The bending stiffness of the soft material of robot body can influence the locomotion performance. In our study, we used a polymer-based resin to 3D

print the robot body. The young's modulus and density of pure resin were known from the material specification, which is 12 MPa and 1.1 kg/m³, respectively. From the literature we compute the young's modulus and density of particle-polymer composite, which are about 454.35 MPa⁵⁰ and 192.1 kg/m³, respectively. These properties were input in our simulation to confirm if the robot body would have sufficient elasticity required to mimic crawling locomotion of an inchworm. Prior research has been conducted where researchers have described strategies to control bending elasticity of 3D printed soft bodies.⁵¹ In future prototypes, we plan to design the thickness distribution of the robot body according to elastic properties and desired bending stiffness for enhanced locomotion performance.

Two permanent magnets with a magnetic field strength of 6269 A/m were placed 0.2 mm beneath the two legs of the robot, as illustrated in Figure 2b. The goal of the simulation was to observe the displacement of the robot body along y and z directions with the displacement of posterior and anterior magnets along y axis. The following equation was used to relate magnetic flux density, magnetic field, and scalar magnetic potential:

$$-\nabla(\mu_0\nabla V_m - \mu_0 M) = 0 \quad (4)$$

where $H = -\nabla V_m$; B is magnetic flux density, H is magnetic field strength, M is magnetization, μ_0 is permeability of medium (air), and V_m is scalar magnetic potential.

The magnetic field was symmetric with respect to the yz plane, in which the magnetic field was tangential to the boundary. This is described by the magnetic insulation condition:

$$n \cdot (\mu_0\nabla V_m - \mu_0 M) = n \cdot B = 0 \quad (5)$$

This boundary condition can be represented with a constant magnetic scalar potential. The simulation model uses a zero-magnetic scalar potential condition. As the air box is

sufficiently large in size, the boundary conditions used on its remaining exterior boundaries have very little influence on the field near the magnet. Although an infinite element domain might give better results, this model uses the magnetic insulation condition for analytical convenience. The overall magnetic force on the robot is calculated as an integral of surface-stress tensor over all boundaries of the robot body.

Experimental Result and Discussion

Simulation result

As illustrated in Figure 4, the simulation results show that the magnetic actuation of the soft robot demonstrated similar body deformation and flexibility as observed in real-life inchworms, mimicking their crawling locomotion successfully. Initially, the magnet 1 moved 3 mm along y axis, while the magnet 2 was stationary. This prompted the robot to move its posterior leg around 2 mm in y axis. As the anterior leg was anchored by the magnet 2, the body bent because of the polymer's flexibility and deformed in z axis due to the magnetic force. The maximum bending deformation was found around 7 mm with a 25° tilt angle. The leg movements were spontaneous with respect to the magnet movement, with no lag observed in the time dependent displacement simulation.

Experimental tests of robot locomotion

The COMSOL simulation demonstrated the feasibility of the linear displacement strategy using magnetic actuators in posterior and anterior legs of the robot. Experiments were conducted using the 3D printed soft robot to validate the simulated movements. A magnetic field strength of 6269 A/m was applied for magnetic actuation, which was induced by two cylindrical NdFeB permanent magnets (rare earth grade N52, from D8C; K&J Magnetics, Inc., PA) with a diameter of 0.25 inch and thickness of 1 inch. The magnetic field was about ~7 mT. A similar magnetic field actuation was conducted in a previous literature,⁵² which used a maximum of

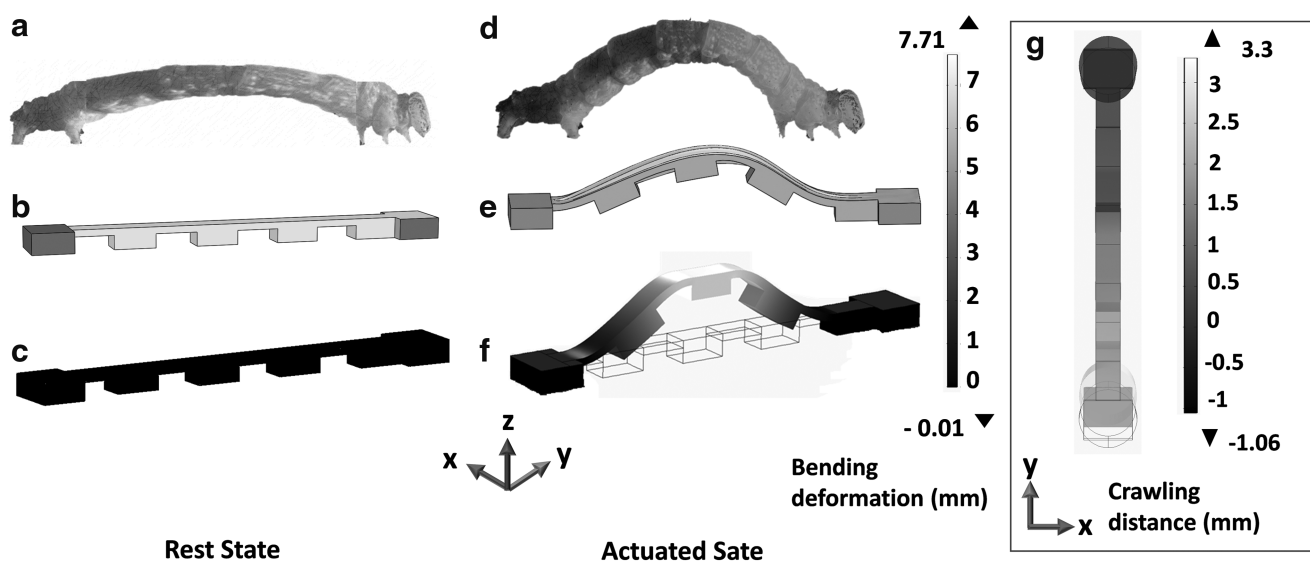


FIG. 4. Displacements of soft robot compared to real-life inchworm in rest state (a–c) and actuated state (d–f). (a, d) real-life inchworm, (b, e) simulated digital model, (c, f) simulation results showing bending deformation, (g) simulation result showing crawling distance in actuated state.

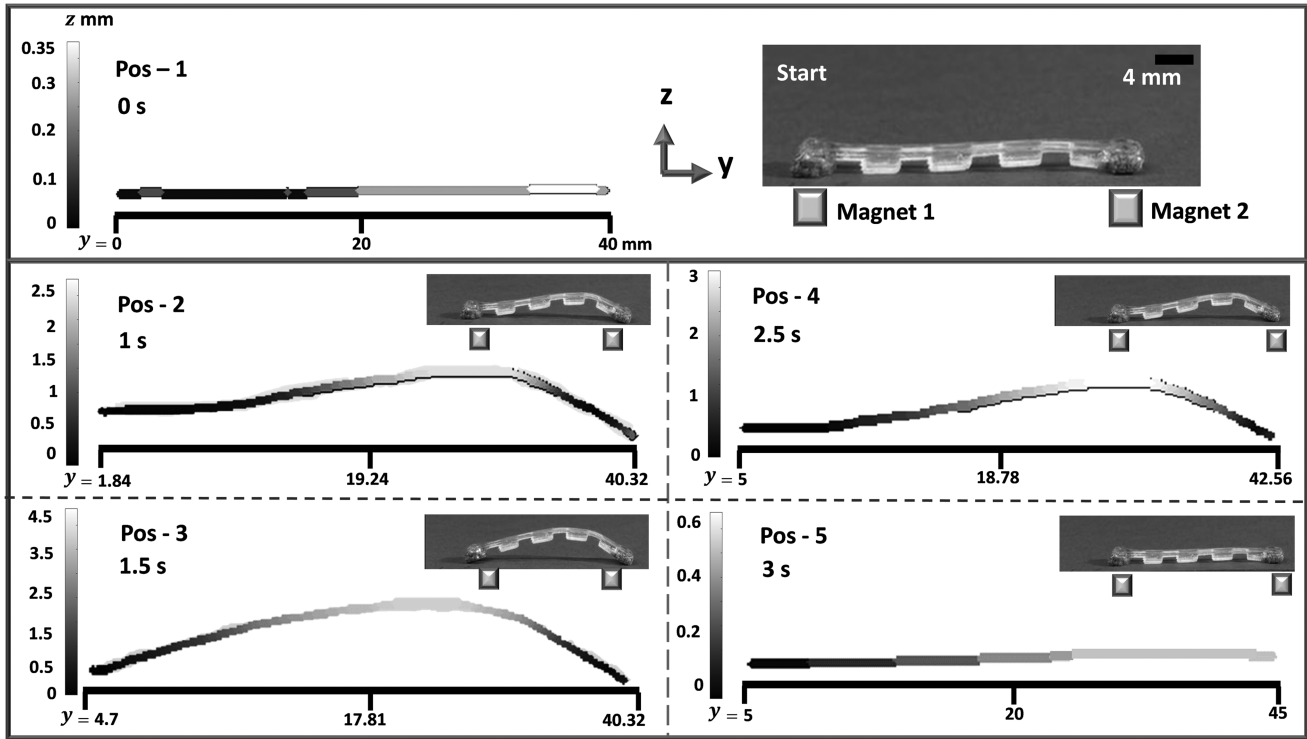


FIG. 5. Linear crawling locomotion and bending deformation in different crawling positions on a construction paper surface with a roughness R_a of $0.6 \mu\text{m}$.

10 mT magnetic field. This limited exposure in a controlled environment is quite safe and under the safety limit.^{53–55} The magnets were placed 0.2 mm beneath the posterior and anterior legs. The substrate was a 0.2 mm thick nonslippery construction paper. The room temperature during the experimental tests was 298.15 K. Figure 5 shows the linear crawling locomotion of the 3D printed robot under the moving magnetic field and the corresponding bending deformation in different crawling positions (pos 1–5). With alternating magnetic actuation, the robot was able to move linearly in y direction with deformation of its body in the z direction. The displacements in y , z direction, threshold angle, and curvature of the robot were measured using MATLAB. With 8 mm movement of the magnet 1, the robot's posterior leg moved 5 mm crawling distance in y direction. The relative movement of the leg with respect to the magnet movement was similar to simulation results, which showed 2 mm crawling distance of the posterior leg with 3 mm movement of magnet 1. A comparison summary of maximum bending deformation, highest curvature and threshold angle for real worm, simulation result, and 3D printed robot is shown in Table 2.

Figure 6a shows the measured crawling distance of posterior and anterior legs of the soft robot, in both simulation and experimental tests. In case of simulation, the two legs had a stride speed of 0.91 mm/s and moved 2 mm after one crawling cycle; the crawling cycle was 2.2 s. For experimental case, both of the legs had a stride speed of 1.67 mm/s and moved ~ 5 mm after one crawling cycle. Each crawling cycle was about 3 s long. In both cases, the posterior and anterior legs moved same distance after one cycle, but the movement and speed were not same in different crawling

positions, because of the alternating movement of magnets and friction states of two legs. Figure 6b compares the curvature at different crawling positions of real-life inchworm, simulated and 3D printed soft robots during crawling locomotion. The curvature values follow similar pattern in all three cases; we observe minimum curvature at crawling position 1 and maximum curvature at position 3. The curvature of real-life inchworm is slightly higher compared to simulated and experimental cases. In addition, we measured the load carrying capacity of the robot in the paper surface. It was observed that the robot can carry a maximum load of 5.95 g, which was almost 30 times of its body mass (0.2 g).

For further testing the locomotion performance of the robot, several experiments were conducted in different scenarios, including crawling inside a complex maze, crawling on a rough sandpaper surface, and climbing on an inclined surface with an angle of 45° with a load. The locomotion experiment videos can be found in Supplementary Video S1. Screenshots of these

TABLE 2. COMPARISON OF BODY LOCOMOTION PARAMETERS

	<i>Max bending deformation (mm)</i>	<i>Highest curvature</i>	<i>Threshold angle (θ_{max}), degree</i>
Real worm	3	1.29	21.5
Simulated	7	1.27	25
3D printed robot	4.5	1.24	12.32

3D, three-dimensional.

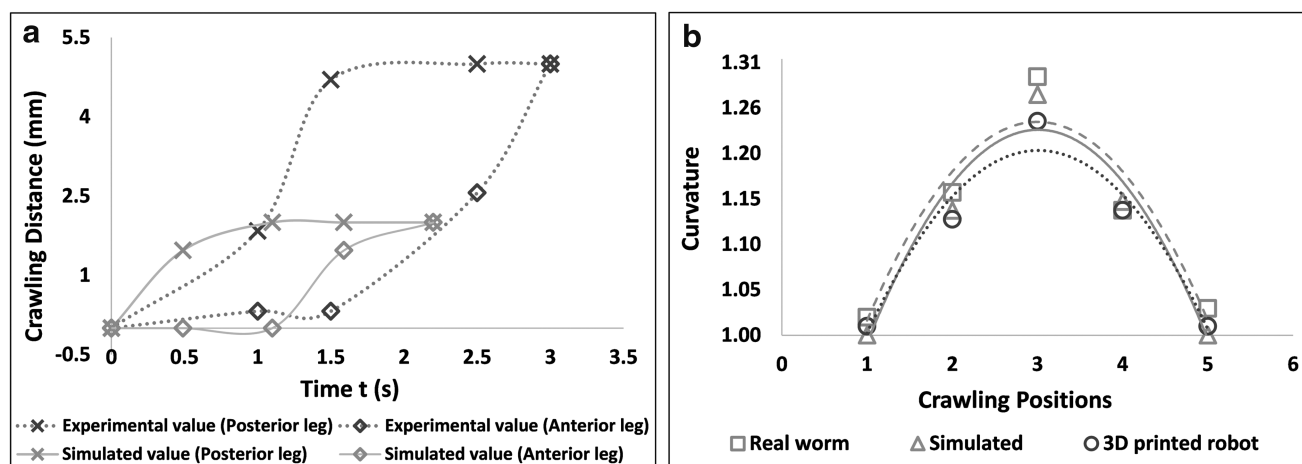


FIG. 6. (a) Crawling distances of posterior and anterior legs of the soft robot in simulation and experimental test on a construction paper surface ($R_a \approx 0.6 \mu\text{m}$), (b) Comparing the curvature at different crawling positions of real-life inchworm, simulated and 3D printed soft robots during crawling locomotion on a construction paper surface ($R_a \approx 0.6 \mu\text{m}$). 3D, three-dimensional.

locomotion videos are shown in Figure 7. As shown in Figure 7a, in the maze, the robot followed the magnetic force from the anterior and posterior magnets and steered accordingly. However, as mentioned before, the bending capability for this prototype is only uniaxial. So turning was limited in a congested space. As shown in Figure 7b, on the sandpaper which has a much higher roughness than the construction paper, the robot faced a higher friction from the substrate, resulting in a lower bending and a slower speed. On an inclined surface, the crawling locomotion maintained the regular speed and bending. In addition, we attached a load with the robot to see if it can carry a weight during climbing on an inclined construction paper surface. We found that the robot can carry a maximum load of 0.38 g, which was 1.5 times of its body mass (0.2 g), while crawling on a 45° inclined surface, as shown in Figure 7c. The substrates in Figure 7a and c are construction paper surface, and the test in Figure 7b was performed on a sandpaper substrate which is relatively rougher. In all tests in this article, the construction paper substrate has a roughness R_a of $0.6 \mu\text{m}$, and the sandpaper substrate has a roughness R_a of $2.5 \mu\text{m}$.

The robot locomotion was further tested in a congested spacing. The robot height was about 2 mm, and the highest deflection of its upper body surface was about 4.5 mm along the z axis. So, the actuation was tested inside a tube with a diameter of 5 mm, made of cellulose acetate sheets. The whole process is illustrated in the Supplementary Video (Supplementary Video S2). Screenshots were taken and shown in Figure 8. It shows that the robot was able to step up from the paper substrate to tube surface with its crawling locomotion and then move through the tube smoothly. The medium inside the tube was air. During the process of stepping to the tube surface from the paper substrate, the crawling cycle slowed down for two to three cycles (6–8 s). But as the robot went inside the tube, the crawling speed actually became faster. Because of the comparatively smooth surface of the tube, the robot faced smaller friction force and took 2.5 s to complete one crawling cycle inside the tube (Fig. 8b). Although the maximum deflection was slightly lower due to the space constraint, the linear movement was not hampered. In our future prototype, we plan to redesign the soft robot

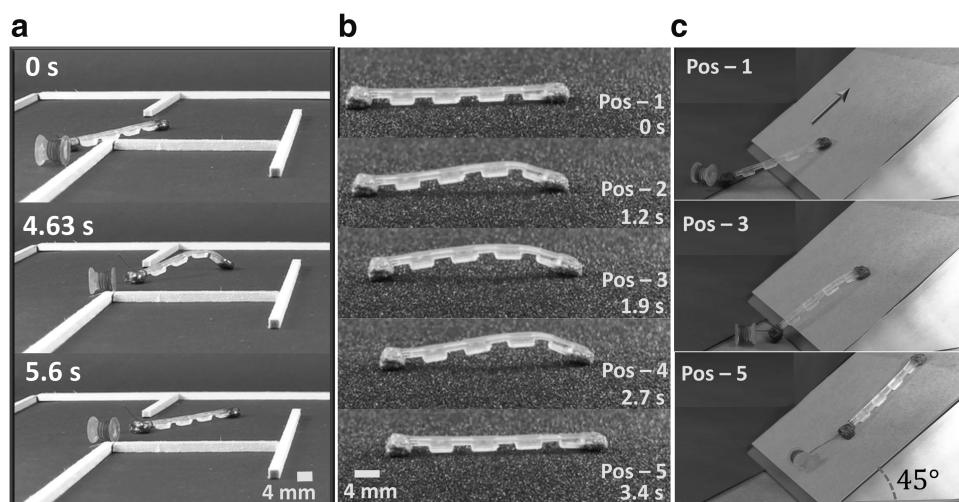
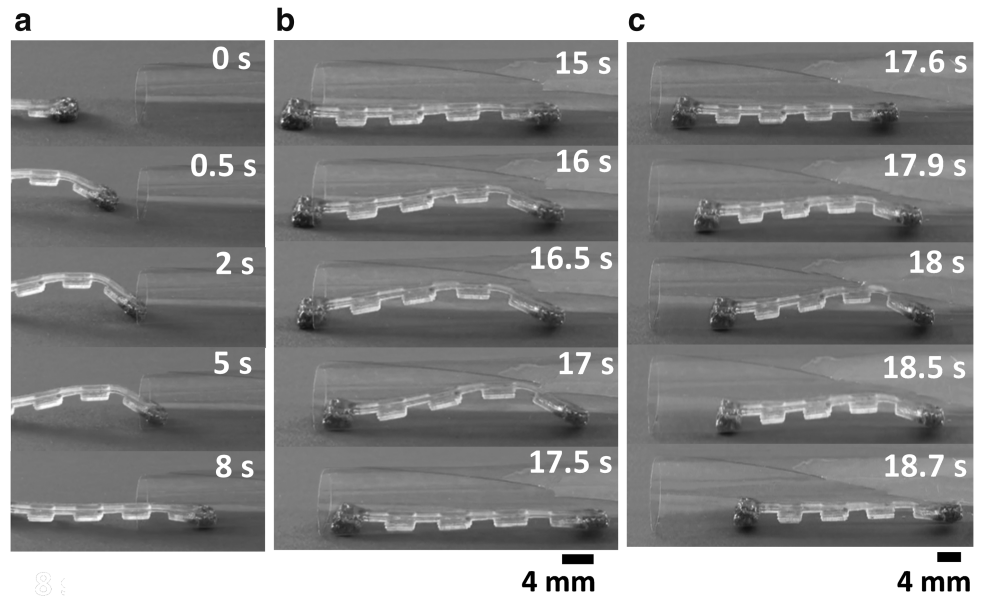


FIG. 7. Locomotion experiments in different scenarios. (a) In a complex maze (construction paper surface: $R_a \approx 0.6 \mu\text{m}$), (b) On a rough surface (sandpaper surface: $R_a \approx 2.5 \mu\text{m}$), and (c) climbing on an inclined wall (construction paper surface: $R_a \approx 0.6 \mu\text{m}$).

FIG. 8. Soft robot crawling locomotion through a congested tube. **(a)** Locomotion cycle while entering the tube, **(b, c)** two cycles inside the tube.



body structure to add biaxial body bending, which will allow sharp turns in congested spaces like curved tunnels as shown in the study by Chao *et al.*⁵²

Friction test

Our designed soft robot uses an actuation system that creates high and low states of friction with the substrate and generates a push–pull steering motion. These alternating states of friction are a function of the tilt angle. To quantitatively demonstrate the relation, the friction force was measured for different tilt angles using the following equation,

$$F_f = \mu F_n \quad (6)$$

where F_f is the friction force exerted on each other by the robot and the substrate, μ is the friction coefficient, an empirical value of the contacting materials, and F_n is the normal force, the perpendicular force exerted by the robot on the substrate. The normal force is influenced by the gravitational force on the robot $G = mg$ ($m = \text{mass}$, $g = \text{gravitational acceleration}$), which can be split into the force pointing down an inclined slope with tilt angle, θ , $G_s = mg \sin(\theta)$ and the force normal to the slope, $G_n = mg \cos(\theta)$. At an incline, G_n is the only normal force being exerted on the surface by the robot. So,

$$F_n = mg \cos(\theta) \quad (7)$$

$$F_f = \mu [mg \cos(\theta)] \quad (8)$$

From Equation (8), we can clearly observe that the friction force is a function of tilt angle, θ , as all the other values are constant. Figure 9 illustrates the friction force exerted on the robot's posterior leg and plots the normalized F_f as a function of the tilt angle in different locomotion positions.

We see from Figure 9 that the friction is the highest when tilt angle is zero, as in when the legs are in resting position. As θ increases, the friction decreases and at maximum tilt angle (threshold angle, θ_{\max}) and highest curvature, the friction

becomes the lowest. At this point, the magnetic force on the posterior or anterior legs switches on/off and the robot moves forward. As the leg goes toward a resting position, the friction starts increasing again until the next crawling cycle.

For simplification, we have just considered friction force exerted in one specific point on the posterior leg. The friction coefficient μ is a constant for the interaction of our 3D printed robot and a specific substrate. So, we normalized the friction force F_f by dividing μ and calibrated the relation of the normalized friction with the inclination angle, as plotted in Figure 9. In Figure 9, we also compared the friction force on a construction paper surface and a rough sandpaper surface. On a rougher substrate such as the sandpaper tested in this study, a higher friction would cause a lower maximum bending of the robot, resulting in a lower crawling speed and a shorter stride length.

Stride efficiency analysis

During the actuation of the soft robot, the posterior and anterior legs alternated their roles for steering and as anchors depending on high and low friction states. The steering leg moved with the influence of the external magnetic force created by the corresponding magnet. However, the leg displacement after one cycle (also be defined as stride length⁵) was not the same as the magnet movement due to various factors such as gravity, friction, and effect of the magnetic field from the other magnet. Quantifying the leg displacement (output) with relation to magnet displacement (input) gives us an overall idea about the locomotion performance and efficiency of the robot. In addition, in our study we simulated the magnetic actuation and based the experimental setup on the simulation results. So, it was also important to analyze how closely the experimental locomotion followed the locomotion characteristics evaluated in the simulation.

An example scenario is illustrated in Figure 10. The posterior leg of the soft robot moved by a distance a_1 as the magnet 1 moved by a distance a_2 . We defined the relation of the leg and magnet displacement as the effective stride length, L_{eff} .

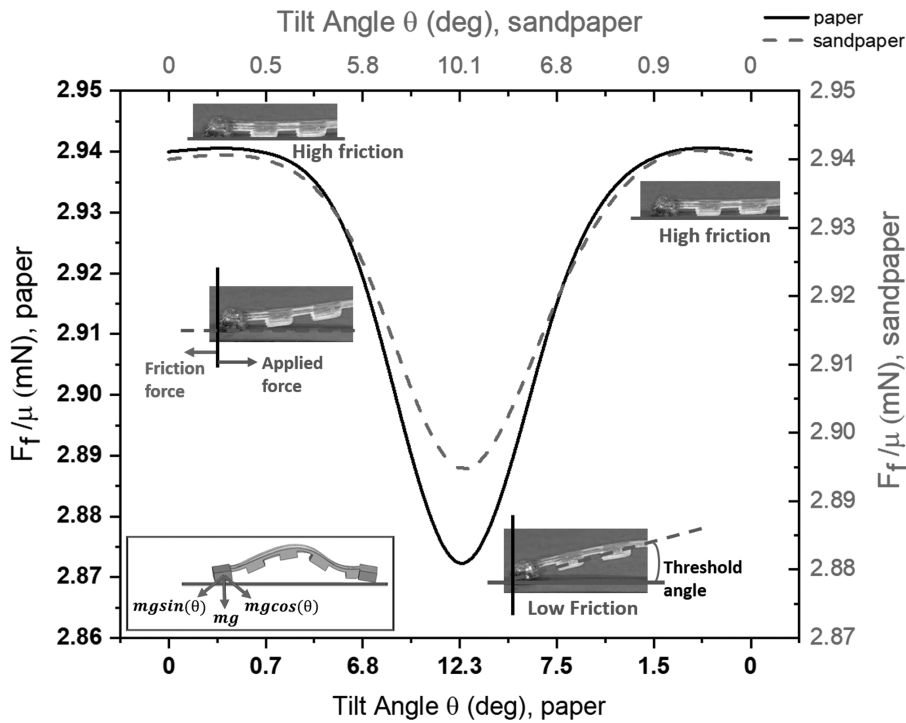


FIG. 9. Normalized friction force as a function of surface inclination angle.

$$L_{eff} = \frac{a_1}{a_2} \tag{9}$$

To test the accuracy of simulation results, the L_{eff} obtained from the COMSOL simulation was compared with the experimental results. From simulation we saw that the legs moved 2 mm as magnet moved 3 mm. And in our experimental result, the legs moved by 5 mm for the magnet displacement of 8 mm. So, we can calculate,

$$L_{eff}(simulation) = \frac{2}{3} = 0.67$$

and

$$L_{eff}(experiment) = \frac{5}{8} = 0.625$$

The locomotion efficiency, η_{eff} , is defined here as the ratio of simulation and experimental effective stride length,

$$\eta_{eff} = \frac{L_{eff}(simulation)}{L_{eff}(experiment)} * 100\% = 93.28\% \tag{10}$$

This implies that, in experimental tests, the robot's locomotion and effective stride length was 93.28% similar to the simulation result obtained in the COMSOL simulations, showing a high agreement between the experimental and simulation results. It further indicates that the 3D printed soft robot could be accurately controlled and programmed using the parameter settings validated in COMSOL simulations.

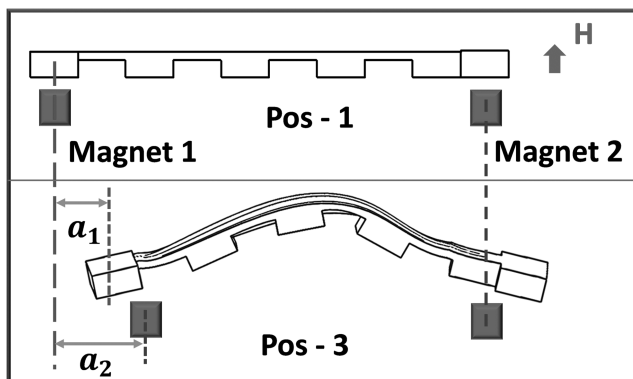


FIG. 10. Analyzing stride length of robot legs.

Conclusions

This study reports the design and fabrication of a fully 3D printed, tetherless, inchworm-inspired biomimetic soft robot. Multimaterial additive manufacturing enables efficient fabrications of the monolithic and flexible composite structure with highly accurate geometry and locally programmed material distribution, without any need of manual assembly or pre-post processing work. The tetherless robot uses a magnetic actuation system, which completely circumvents the intrinsic issues associated with different hydraulic, pneumatic, and SMA based actuators. Magnetic actuation, in association with smaller dimensions, allows the robot to maneuver in tiny spaces with significantly smaller stride length. The robot is lightweight, noise free, and highly deformable. It uses an anchor push-anchor pull locomotion strategy mimicking the inchworm and is capable of two-way linear actuation. The robot demonstrates a stride length of 5 mm, which is about one eighth of its body length, with a linear speed of 1.67 mm/s and a linear locomotion efficiency of 93.28% with a maximum bending deformation of 4.5 mm

in z direction. The maximum load carrying capacity on a smooth surface is 5.95 g, which is about 30 times its own mass. It is also able to carry a load 1.5 times of its body weight while stably climbing on a 45° inclined surface. The experimental locomotion of the printed robot agreed well with the simulation results in COMSOL Multiphysics. The locomotion performances of the 3D printed robot are comparable to state of the art, and the use of multimaterial 3D printing technique allows simple, fast, accurate, and assembly-free production of the robot. With its flexible and compliant structure, the fully 3D printed soft robot has potential applications in rescue and reconnaissance applications where large rigid robots are not capable of access.

Future work will focus on improvement of the mobility of the robot and developing turning locomotion functionalities. Extending these concepts to more complex geometry and multimaterial architectures using additive manufacturing would enable efficient fabrication of soft robots with more elaborate and programmable motions.

Author Disclosure Statement

No competing financial interests exist.

Supplementary Material

Supplementary Video S1

Supplementary Video S2

References

1. Trimmer B. A Journal of Soft Robotics: Why Now?. NY: Mary Ann Liebert, Inc., 2014.
2. Li G, Li W, Zhang J, *et al.* Analysis and design of asymmetric oscillation for caterpillar-like locomotion. *J Bionic Eng* 2015;12:190–203.
3. Fang G, Matte C-D, Kwok T-H, *et al.* Geometry-based direct simulation for multi-material soft robots. In: 2018 IEEE International Conference on Robotics and Automation (ICRA), Queensland, Australia: IEEE, 2018:1–6.
4. Lin H-T, Leisk GG, Trimmer B. GoQBot: a caterpillar-inspired soft-bodied rolling robot. *Bioinspir Biomim* 2011;6:026007.
5. Wang W, Lee J-Y, Rodrigue H, *et al.* Locomotion of inchworm-inspired robot made of smart soft composite (SSC). *Bioinspir Biomim* 2014;9:046006.
6. Umedachi T, Vikas V, Trimmer B. Softworms: the design and control of non-pneumatic, 3D-printed, deformable robots. *Bioinspir Biomim* 2016;11:025001.
7. Koh J-S, Cho K-J. Omega-shaped inchworm-inspired crawling robot with large-index-and-pitch (LIP) SMA spring actuators. *IEEE/ASME Trans Mechatron* 2013;18:419–429.
8. Rheuben M, Kammer A. Comparison of slow larval and fast adult muscle innervated by the same motor neurone. *J Exp Biol* 1980;84:103–118.
9. Dorfmann A, Trimmer B, Woods W. A constitutive model for muscle properties in a soft-bodied arthropod. *J Royal Soc Interface* 2007;4:257–269.
10. Lin H-T, Slate DJ, Paetsch CR, *et al.* Scaling of caterpillar body properties and its biomechanical implications for the use of a hydrostatic skeleton. *J Exp Biol* 2011;214:1194–1204.
11. Laschi C, Cianchetti M. Soft robotics: new perspectives for robot bodyware and control. *Front Bioeng Biotechnol* 2014;2:3.
12. Koh J-S, Cho K-J. Omegabot: biomimetic inchworm robot using SMA coil actuator and smart composite microstructures (SCM). In: 2009 IEEE International Conference on Robotics and Biomimetics (ROBIO), Guilin, China: IEEE, 2009:1154–1159.
13. Lee D, Kim S, Park Y-L, *et al.* Design of centimeter-scale inchworm robots with bidirectional claws. In: 2011 IEEE International Conference on Robotics and Automation (ICRA), Shanghai, China: IEEE, 2011:3197–3204.
14. Villanueva A, Smith C, Priya S. A biomimetic robotic jellyfish (Robojelly) actuated by shape memory alloy composite actuators. *Bioinspir Biomim* 2011;6:036004.
15. Shepherd RF, Ilievski F, Choi W, *et al.* Multigaît soft robot. *Proc Natl Acad Sci U S A* 2011;108:20400–20403.
16. Stokes AA, Shepherd RF, Morin SA, *et al.* A hybrid combining hard and soft robots. *Soft Robot* 2014;1:70–74.
17. Yang Y, Chen Y, Li Y, *et al.* Bioinspired robotic fingers based on pneumatic actuator and 3D printing of smart material. *Soft Robot* 2017;4:147–162.
18. Zou J, Lin Y, Ji C, *et al.* A reconfigurable omnidirectional soft robot based on caterpillar locomotion. *Soft Robot* 2018;5:164–174.
19. Onal CD, Rus D. Autonomous undulatory serpentine locomotion utilizing body dynamics of a fluidic soft robot. *Bioinspir Biomim* 2013;8:026003.
20. Zatopa A, Walker S, Menguc Y. Fully soft 3D-printed electroactive fluidic valve for soft hydraulic robots. *Soft Robot* 2018;5:258–271.
21. Vikas V, Cohen E, Grassi R, *et al.* Design and locomotion control of a soft robot using friction manipulation and motor-tendon actuation. *IEEE Trans Robot* 2016;32:949–959.
22. Wang C, Sim K, Chen J, *et al.* Soft ultrathin electronics innervated adaptive fully soft robots. *Adv Mater* 2018;1706695.
23. Gelebart AH, Mulder DJ, Varga M, *et al.* Making waves in a photoactive polymer film. *Nature* 2017;546:632.
24. Must I, Kaasik F, Põldsalu I, *et al.* Ionic and capacitive artificial muscle for biomimetic soft robotics. *Adv Eng Mater* 2015;17:84–94.
25. Kim H-J, Song S-H, Ahn S-H. A turtle-like swimming robot using a smart soft composite (SSC) structure. *Smart Mater Struct* 2012;22:014007.
26. Mazzolai B, Margheri L, Cianchetti M, *et al.* Soft-robotic arm inspired by the octopus: II. From artificial requirements to innovative technological solutions. *Bioinspir Biomim* 2012;7:025005.
27. Marchese AD, Onal CD, Rus D. Autonomous soft robotic fish capable of escape maneuvers using fluidic elastomer actuators. *Soft Robot* 2014;1:75–87.
28. Miriyev A, Stack K, Lipson H. Soft material for soft actuators. *Nat Commun* 2017;8:596.
29. Ueno S, Takemura K, Yokota S, *et al.* An inchworm robot using electro-conjugate fluid. In: 2012 IEEE International Conference on Robotics and Biomimetics (ROBIO), Guangzhou, China: IEEE, 2012:1017–1022.
30. Lee H, Kim J, Kim J, *et al.* Programming magnetic anisotropy in polymeric microactuators. *Nat Mater* 2011;10:747.
31. Cugat O, Delamare J, Reyne G. Magnetic micro-actuators and systems (MAGMAS). *IEEE Trans Magn* 2003;39:3607–3612.
32. Saga N, Nakamura T. Development of a peristaltic crawling robot using magnetic fluid on the basis of the locomotion mechanism of the earthworm. *Smart Mater Struct* 2004;13:566.

33. Mezoff S, Papastathis N, Takesian A, *et al.* The biomechanical and neural control of hydrostatic limb movements in *Manduca sexta*. *J Exp Biol* 2004;207:3043–3053.
34. Mukherjee R, Vaughn S, Trimmer BA. The neuromechanics of proleg grip release. *J Exp Biol* 2018;221:jeb.173856.
35. Van Griethuijsen L, Trimmer B. Locomotion in caterpillars. *Biol Rev* 2014;89:656–670.
36. Lin HT, Trimmer BA. The substrate as a skeleton: ground reaction forces from a soft-bodied legged animal. *J Exp Biol* 2010;213:1133–1142.
37. Metallo C, Trimmer BA. Orientation-dependent changes in single motor neuron activity during adaptive soft-bodied locomotion. *Brain Behav Evolut* 2015;85:47–62.
38. Trimmer B, Issberner J. Kinematics of soft-bodied, legged locomotion in *Manduca sexta* larvae. *Biol Bull* 2007;212:130–142.
39. Saunders F, Golden E, White RD, *et al.* Experimental verification of soft-robot gaits evolved using a lumped dynamic model. *Robotica* 2011;29:823–830.
40. Lu L, Joyee EB, Pan Y. Correlation between microscale magnetic particle distribution and magnetic-field-responsive performance of three-dimensional printed composites. *J Micro Nano Manuf* 2018;6:010904.
41. Goh GL, Agarwala S, Yong WY. 3D printing of microfluidic sensor for soft robots: a preliminary study in design and fabrication. In: 2016 2nd International Conference on Pro-AM Progress in Additive Manufacturing (Pro-AM 2016), Singapore: Research Publishing, 2016:177–181.
42. Park Y-L, Chen B-R, Wood RJ. Design and fabrication of soft artificial skin using embedded microchannels and liquid conductors. *IEEE Sens J* 2012;12:2711–2718.
43. Rus D, Tolley MT. Design, fabrication and control of soft robots. *Nature* 2015;521:467.
44. Lu L, Guo P, Pan Y. Magnetic-field-assisted projection stereolithography for three-dimensional printing of smart structures. *J Manuf Sci Eng* 2017;139:071008.
45. Radhakrishnan V. Locomotion: dealing with friction. *Proc Natl Acad Sci U S A* 1998;95:5448–5455.
46. Aguilar J, Zhang T, Qian F, *et al.* A review on locomotion robotics: the study of movement at the intersection of robotics, soft matter and dynamical systems. *Rep Prog Phys* 2016;79:110001.
47. Renda F, Cianchetti M, Giorelli M, *et al.* A 3D steady-state model of a tendon-driven continuum soft manipulator inspired by the octopus arm. *Bioinspir Biomim* 2012;7:025006.
48. Trivedi D, Lotfi A, Rahn CD. Geometrically exact models for soft robotic manipulators. *IEEE Trans Robot* 2008;24:773–780.
49. Antman SS. Problems in nonlinear elasticity. In: *Nonlinear Problems of Elasticity. Applied Mathematical Sciences*. New York, NY: Springer; 2005:513–584.
50. Ouglova A, Berthaud Y, François M, *et al.* Mechanical properties of an iron oxide formed by corrosion in reinforced concrete structures. *Corros Sci* 2006;48:3988–4000.
51. Zhang X, Le X, Wu Z, *et al.* Data-driven bending elasticity design by shell thickness. *Computer Graphics Forum: Wiley Online Library* 2016:157–166.
52. Chao Q, Yu J, Dai C, *et al.* Steering micro-robotic swarm by dynamic actuating fields. In: 2016 IEEE International Conference on Robotics and Automation (ICRA), Stockholm, Sweden: IEEE, 2016:5230–5235.
53. World Health Organization. Electromagnetic fields and public health. *Revista Panamericana de Salud Pública (OPS)=Pan American Journal of Public Health (PAHO)* 1998;3:206–207.
54. World Health Organization. Environmental Health Criteria 232. Static fields. Geneva: World Health Organization, 2006.
55. Leszczynski D. Rapporteur report: cellular, animal and epidemiological studies of the effects of static magnetic fields relevant to human health. *Prog Biophys Mol Biol* 2005;87:247–253.

Address correspondence to:

Yayue Pan
 Department of Mechanical & Industrial Engineering
 University of Illinois at Chicago (UIC)
 842W Taylor Street, ERF 3025
 Chicago, IL 60607

E-mail: yayuepan@uic.edu